JGR Space Physics

RESEARCH ARTICLE
10.1029/2020JA028852

Special Section:
Cluster 20th anniversary: results from the first 3D mission

Heavy Metal and Rock in Space: Cluster RAPID Observations of Fe and Si

Stein Haaland[1,2,3], **Patrick W. Daly**[1], **and Esa Vilenius**[1]

[1]Max-Planck Institute for Solar Systems Research, Göttingen, Germany, [2]Birkeland Centre for Space Science, University of Bergen, Bergen, Norway, [3]The University Centre in Svalbard, Longyearbyen, Svalbard

Key Points:

- A new data product from the Cluster mission is utilized to study heavy ions in geospace
- Traceable amounts of silicon (Si) and iron (Fe) are found in all regions of space traversed by Cluster
- The detected Si and Fe are most likely of solar wind origin

Correspondence to:
S. Haaland,
Stein.Haaland@uib.no

Citation:
Haaland, S., Daly, P. W., & Vilenius, E. (2021). Heavy metal and rock in space: Cluster RAPID observations of Fe and Si. *Journal of Geophysical Research: Space Physics*, *126*, e2020JA028852. https://doi.org/10.1029/2020JA028852

Received 21 OCT 2020
Accepted 8 FEB 2021

Abstract Metallic and silicate ions carry essential information about the evolution of the Earth and near-Earth small bodies. Despite this, there has so far been very little focus on ions with atomic masses higher than oxygen in the terrestrial magnetosphere. In this paper, we report on abundances and properties of energetic ions with masses corresponding to that of silicon (Si) and iron (Fe) in Earth's geospace. The results are based on a newly derived data product from the Research with Adaptive Particle Imaging Detectors on Cluster. We find traces of both Si and Fe in all of the regions covered by the spacecraft, with the highest occurrence rates and highest intensities in the inner magnetosphere. We also find that the Fe and Si abundances are modulated by solar activity. During solar maximum, the probability of observing Fe and Si in geospace increases significantly. On the other hand, we find little or no direct correlation between geomagnetic activity and Si and Fe abundance in the magnetosphere. Both Si and Fe in the Earth's magnetosphere are inferred to be primarily of solar wind origin.

1. Introduction

Knowledge about composition of matter in space is important for assessing formation and evolution of planets and their habitability. Heavy ions and molecular ions are also trace particles and can provide information about transport of matter through space and across boundaries. Identifying the source and supply routes of matter tells us about re-distribution and migration of matter through space into the planetary and cometary system for short time scales and about planetary formation and evolution on geological time scales.

Most recent space missions to other planets are therefore equipped with instrumentation capable of measuring the composition of the planet's neutral gas or plasma environment (Geiss et al., 1992; P. R. Young, 2005; Zurbuchen et al., 2011). The technique varies from remote sensing using optical measurements and spectrography (see e.g., overview in Huber et al., 2010) to in-situ measurements using particle detectors (see e.g., overview in Wüest et al., 2007), but the purpose is often the same; determine the composition of the planet, its atmosphere, and its plasma (and dust) environment in order to understand processes and planetary evolution.

Composition is also a primary science objective for most missions to cometary bodies. The International Sun-Earth Explorer-3 (ISEE-3; later renamed to International Comet Explorer, ICE) satellite, originally designed to study the solar wind, was the first spacecraft mission to probe the plasma vicinity of comet (Giacobini-Zinner) in 1985 (Cowley, 1985). Later, the French/Soviet Vega probes, Vega 1 and 2 (e.g., Fomenkova et al., 1989; Sagdeev et al., 1986; Werner et al., 1989) as well as the European Space Agency (ESA) Giotto mission (e.g., Kissel et al., 1986; Reinhard, 1986) sampled the vicinity of comet Halley. The latter had a dedicated heavy ion particle spectrometer (Korth et al., 1987; Wilken et al., 1987). Composition was also prime objectives of later missions like Hayabusa (Nakamura et al., 2011; Okada et al., 2006), Stardust (Brownlee et al., 2003), and Rosetta (e.g., Gulkis & Alexander, 2008; Heritier et al., 2017; Le Roy et al., 2015).

Composition measurements were also considered a prime scientific objective already in the first missions to explore the solar wind. The first in-situ composition measurements were inferred from depositions in metallic foils retrieved after exposure to the pristine solar wind (e.g., Geiss et al., 1970; Eberhardt et al., 1972). Later missions, for example, Ulysses (Geiss et al., 1995; Gloeckler et al., 1992; von Steiger et al., 2000; von Steiger & Zurbuchen, 2002) had dedicated particle instruments capable of measuring composition. Consequently, we have a fairly good overview of the composition of various ions species and their charge states

in the solar wind as well as their time variations in response to, for example, coronal mass ejections (e.g., Gilbert et al., 2012; Mitchell et al., 1983; Zurbuchen et al., 2016) or solar energetic proton events (e.g., Reames et al., 1994) on short time scales, and long term solar cycle variations (e.g., von Steiger et al., 1997; Zurbuchen et al., 2002).

The Earth's atmosphere is also well mapped when it comes to composition (e.g., Hollingsworth et al., 2008; Inness et al., 2019; Istomin, 1963). Charged constituents, predominantly confined to the ionosphere, primarily consist of protons, singly ionized oxygen (O^+) and molecular N_2^+ (Bilitza et al., 2017). Ionization is mainly due to solar radiation in the short wavelength part of the solar spectrum, though particle precipitation and cosmic rays also contribute. The same processes can also ionize molecules like, for example, O_2^+, NO^+, though the ionization energy is generally higher than for atoms (for an overview, see e.g., Solomon, 1991).

Even metallic and silicate ions such as iron (Fe), magnesium (Mg), silicon (Si), and sulfur (S) can be found in the terrestrial ionosphere (e.g., Aikin & Goldberg, 1973; Kopp, 1997; Kumar & Hanson, 1980). Most of these ions are the result of meteor ablation in the lower part of the atmosphere (e.g., Campbell-Brown, 2019; Plane et al., 1999), but heavy ions of solar wind origin can also be found (e.g., Fritz et al., 2003; Grande et al., 1996; Perry et al., 2000). Another, and increasing, source of metallic and silicate ions in near-Earth space is fragmentation of debris from artificial satellites (ESA, 2020; Kessler & Cour-Palais, 1978).

The terrestrial magnetosphere contains a mixture of ions of both atmospheric and solar wind origin. For light ions of solar wind origin (H^+ and He^{++}) and terrestrial atomic volatiles (H^+, He^+, and O^+), the circulation, energization, and their impact on magnetospheric dynamics have been extensively studied since their discovery half a century ago (Shelley et al., 1972). The role of the ionosphere as a source of plasma for the magnetosphere has also been extensively studied (e.g., Chappell et al., 1987; Yau & Andre, 1997).

Somewhat surprisingly, the role of ions heavier than oxygen and the overall composition of the terrestrial magnetosphere have received little attention, and observations of heavy ions and molecular ions are sparse. This can partly be explained by the fact that magnetospheric physics traditionally has had a strong focus on the dynamics due to solar wind-magnetosphere and magnetosphere-ionosphere interactions (space weather). The role of molecular ions and metallic and silicate ions are of little or no relevance for such effects, and the composition aspect of the magnetosphere has therefore primarily focused on the lighter ions and oxygen, which have a more direct effect on the geoactivity. Another explanation for the lack of observations is constraints in instrumentation. For the solar corona (and the solar wind) and the Earth's atmosphere, optical emissions have provided a wealth of composition information, but this methodology is poorly suited to probe the magnetosphere.

To our knowledge, a mission with dedicated instrumentation for composition measurements with the exploration of silicate and metallic ions in Earth's geospace as a prime objective has not been flown. However, existing instrumentation from past and on-going missions are often capable of detecting heavy ions and molecular ions. For example, Klecker et al. (1986) reported observations of molecular ions in the inner magnetosphere during disturbed geomagnetic conditions. Likewise, Christon et al. (1994) reported on molecular ions of ionospheric origin in the deep magnetotail from the Suprathermal Ion Composition Spectrometer (STICS) onboard the Geotail spacecraft during disturbed conditions. Poppe et al. (2016) found molecular ions near the moon in Artemis measurements, presumably originating from sputtering off the moon surface.

More recently, Christon et al. (2017) also reported the discovery of low charge state metallic ions (Fe^+) in the Earth's magnetosphere using the Geotail STICS instrument. The low charge state indicates an ionospheric origin, and Christon et al. (2017) argued that the detected ions were the result of meteorite ablation in the Earth's mesosphere (Plane et al., 1999), followed by upward and outward transport. Observations of Fe of solar wind origin inside the magnetosphere have also been reported by, for example, Fritz et al. (2003) and more recently by Haaland et al. (2020).

In this paper, we follow up on and extend the study of Haaland et al. (2020) by utilizing a new set of measurements from the Research with Adaptive Particle Imaging Detectors (RAPID) on Cluster. In particular, we investigate the occurrence and abundance of ions with atomic masses around that of silicon (Si) and

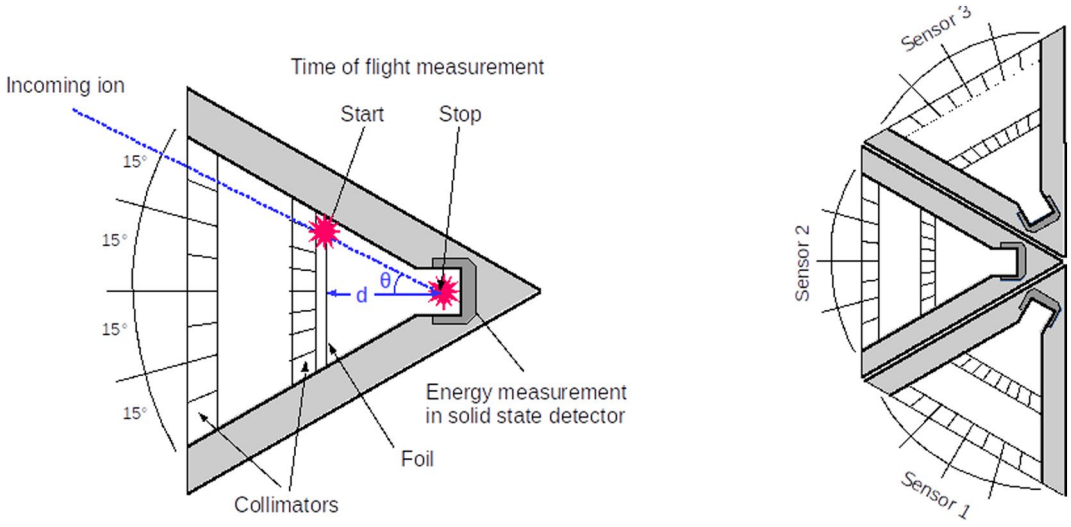

Figure 1. Left: Schematic illustration of a RAPID IIMS sensor head. The time-of-flight (TOF) is generated from a start signal, generated by electrons emitted when the incoming ion passes the start foil, and a stop signal is generated by electrons when the ion hits the surface of the solid state detector. From the known travel distance (d = 32–37 mm, depending on incidence angle, θ), the velocity of the ion can be detected. Combined with the energy, the ion species (but not their charge state) can be determined. Right: Illustration of three sensor heads combined to cover 0–180° elevation. The satellite spin is utilized to get the full 360° azimuthal coverage needed for full 3-dimensional distribution functions. Adapted from Haaland et al. (2020). IIMS, Imaging Ion Mass Spectrometer; RAPID, Research with Adaptive Particle Imaging Detectors; TOF, time-of-flight.

iron (Fe) in various regions of geospace as well as their spectral characteristics and variation with solar cycle and geomagnetic activity.

This paper is organized as follows. In Section 2, we outline the detection principle and processing of the measurements. In Section 3, we provide an overview of the observations and provide characteristics of Si and Fe ions in various regions of space. Section 4 discusses time variations in Si and Fe abundance as function of solar and geomagnetic activity. Finally, Section 5 summarizes the results of this study.

2. Detection of Heavy Ions

Here, we briefly describe the measurement principle and data products for the present study. For further details about the instruments and measurements mode, we also refer to Wilken et al. (1997) as well as the Cluster RAPID calibration report (Kronberg et al., 2020).

2.1. Detection Principle: E-TOF

Composition determination in the RAPID Imaging Ion Mass Spectrometer (IIMS) instrument relies on a combination of time-of-flight (TOF) of a particle, and its measured energy (E). This is schematically illustrated in Figure 1. An incoming ion will first pass a thin foil where an electronic 'start' signal is given. A second 'stop' signal is emitted when the particle hits the solid state detector, where its remaining energy is measured. The combination of energy and time-of-flight (an E-TOF event) can be used to determine the particle's mass, and thus its species. The Cluster RAPID detector system does not have any electrostatic deflectors, so it is not possible to determine charge state of the incoming ions.

While conceptually simple, there are in practice a couple of pitfalls and caveats with this methodology, in particular, related to the identification of particles based on their mass. There are also issues related to energy losses in the TOF system and the solid state detector that causes a fairly high energy detection threshold. Due to these detector losses, neither the measured energy nor the derived velocity are those of the incoming particle. Knowledge about detector losses are therefore required to fully characterize an incoming particle. Due to Coloumb forces, heavy ions also suffer strong angular scattering when interacting with the atoms

of the start foil (e.g., Meyer et al., 1977; Stüdemann & Wilken, 1982). Consequently, a fraction of the incident ions will be scattered out of the flight path of the TOF detector, thus reducing the overall detection efficiency.

On an atomic level, masses of elementary particles are quantized, and not all species are present in space. The most common ion species in geospace is hydrogen (i.e., a proton) and has an atomic mass (AMU) of 1. The second lightest ion species, helium (which nuclei consists of two protons and two neutrons in its most abundant isotope), has mass 4 AMU, that is, 4 times the mass of hydrogen. In Earth's geospace, both these species can originate from either the solar wind or the Earth's atmosphere. Due to the large mass difference, H and He occupy very different locations in the E-TOF space, and are easy to distinguish from each other.

The third most abundant ion species in geospace, oxygen (16 AMU), is primarily of atmospheric origin. In terms of mass and thus identification from RAPID measurements, oxygen is also well separated from the much lighter hydrogen and helium ions. However, the terrestrial atmosphere also contains significant abundances of nitrogen and carbon (12 and 14 AMU in their most abundant isotopes, respectively). These masses are close to that of oxygen, and the RAPID sensor is not able to distinguish between these three species (Wilken et al., 1997). In the science products from RAPID, oxygen is therefore sometimes referred to as "CNO" with the provision that the observed particle can be either C,N, or O.

A further complication arises from the fact that not only atomic matter, but also molecular ions can exist in geospace. For example, carbon, nitrogen, and oxygen in various molecular forms, for example, N_2, O_2, NO, CO, CH_4 with masses in the range 18–32 AMU and NO_2 and CO_2 with masses in the range 44–46 AMU, are abundant in the atmosphere, and can leak out into space (e.g., Dandouras, 2020). Being predominantly of atmospheric origin, these will typically have a much lower initial energy than the energy threshold of the data product we use in the present study, so misidentification is less of an issue. In the RAPID detector, disintegration of molecules may occur and the fragments can have slightly different velocities as well as different scattering angles when they leave the foil (Wilken & Stüdemann, 1984).

2.2. Previous Attempt to Study Heavy Ions: RAPID DE Observations

In RAPID, E-TOF space is represented as a 256×256 matrix. Telemetry constrains prevent transmission of each individual E-TOF event, or the full E-TOF matrix integrated over some time interval. Instead, onboard algorithms accumulate counts over various areas in E-TOF space and calculate count rates which are then converted to fluxes on ground. However, for a limited number of events per spin, the measured energy and time-of-flight information, along with directional information (elevation angle and spin sector) are available as a *diagnostics* product from the RAPID instrument. A prioritization scheme ensures that information about ions with high masses are transmitted first, while ions mapping to E-TOF combinations corresponding to hydrogen, helium, and oxygen come later in the output queue. This product, termed Direct Events (DE), was utilized in Haaland et al. (2020) to study the distribution of energetic Fe in geospace.

Separation between species in E-TOF space is based on simulations of the RAPID sensor system responses using the Stopping and Range of Ions in Matter (SRIM) algorithms described in Ziegler et al. (2010). Basically, this procedure estimates the atomic mass of a given particle based on its E-TOF combination, and takes into account energy losses in the TOF systems and the solid state detectors of the RAPID IIMS sensor units.

Figure 2a shows an example of an E-TOF matrix with DEs accumulated over a 17 h time interval. The lighter ions and CNO line up along their expected (from the SRIM simulations) locations in E-TOF space, albeit with some spread due to varying incidence angles. One can also see clear signatures of ions with mass corresponding to that of Fe ($\simeq$56 AMU), whereas ions with masses around that of Si ($\simeq$28 AMU) are faintly suggested in this DE plot.

For simplicity, we will hereafter refer to particles occupying these regions of E-TOF space as Si and Fe, respectively, rather than repeating formulations like "masses around" or "masses corresponding to". The resolution of RAPID does not allow an exact determination of a particle's AMU, and one cannot exclude the possibility that signals around this region of E-TOF space can be species other than Si and Fe. In particular, magnesium (Mg, $\simeq$24 AMU) can sometimes be almost as abundant as Si in the solar wind, and

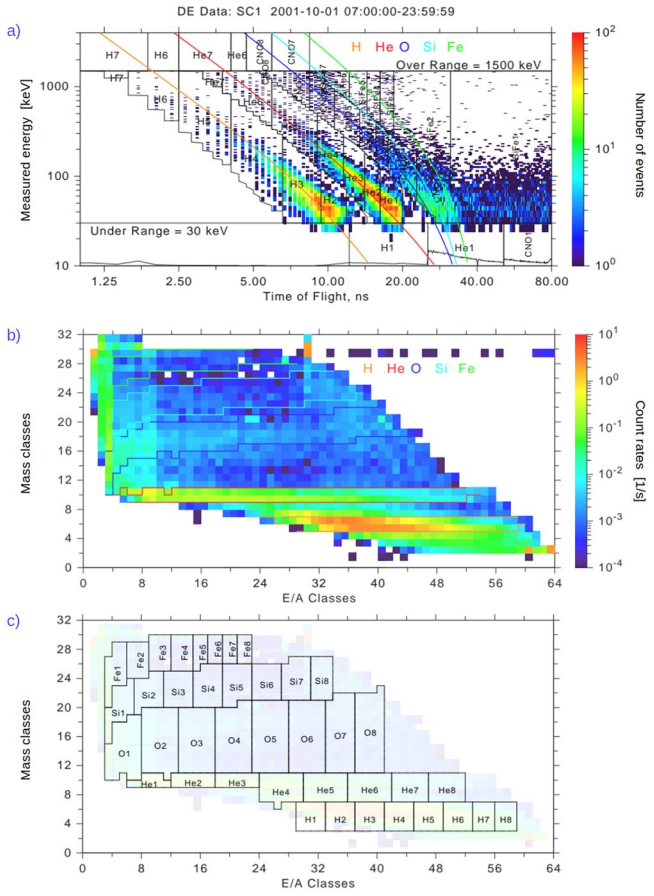

Figure 2. Panel (a): Illustration of the E-TOF matrix, here with DEs accumulated over a period of 17 h on October 1, 2001. Color indicate number of counts, the vertical axis indicates energy as measured in the solid state detector, and the horizontal axis shows the time-of-flight. Black lines show pre-defined separations between species and energies hard-coded in the onboard processing units (DPU) of the instrument. Colored lines show the locus of five ions species, as re-calculated using an updated version of the SRIM software with actual foil and detector characteristics for RAPID, and assuming an incidence angle (θ in Figure 1) of 15°. Panel (b): MTRX data for the same time interval, with 32 mass bins (vertical scale) and 64 energy-per-mass bins (E/A classes; horizontal scale). Color now indicate count rates, with colored lines indicating SRIM curves for the limiting incidence angles of 0° and 30°. Panel (c): The 5 × 8 boxes of the RMTRX. This figure is adapted from the RAPID Calibration Report (Kronberg et al., 2020), where similar plots can be found in full size and with extensive explanations. DE, Direct Event; E-TOF, energy and time-of-flight; MTRX, matrix; RAPID, Research with Adaptive Particle Imaging Detectors; SRIM, Stopping and Range of Ions in Matter.

molecules like e.g., N_2, NO, and O_2 (≃28–32 AMU) with high energies have been detected in the ring current during disturbed conditions (Klecker et al., 1986; Seki et al., 2019).

The prioritization scheme and limited number of DE records per telemetry frame did not allow us to construct meaningful energy spectra. Furthermore, since the DE data product was intended for diagnostics of the sensor system, it was never calibrated, and not intended to be used for science. Until recently, the on-board calculated fluxes of hydrogen, helium and CNO were therefore the only science products from RAPID publicly available and stored in the Cluster Science Archive (Laakso et al., 2010).

The success of Haaland et al. (2020) to derive useful science from an uncalibrated diagnostics product lead the RAPID core team to investigate further opportunities to access information about heavy ions (atomic mass above that of O+).

2.3. New Approach: RAPID MTRX Measurements

In addition to the limited number of Direct Events, there is another product in the raw RAPID data that can access the higher mass species. In the RAPID documentation (Daly & Kronberg, 2020; Kronberg et al., 2020), this is referred to as the ion matrix product (MTRX) and is a transformed version of the E-TOF matrix, accumulated over a long time interval and with reduced energy and time-of-flight resolution. Our new approach to investigate heavy ions in geospace is based on a variant of this data product.

Unlike DE's, which contains full information (energy, time of flight, and direction) for a few individual events, MTRX is a re-mapped version of the original 256 × 256 E-TOF matrix with count rates accumulated in a 32 (masses) by 64 (energy-per-mass bins) matrix. There is no directional information, but unlike DE's, *all* events are stored. The accumulation time of a single MTRX sample is 64 spins (approximately 4 min).

Figure 2b shows count rates (but now all counts and directions, not only the prioritized DEs illustrated in panel (a)) from the same October 1, 2001 interval, organized into the 32 × 64 MTRX format. SRIM curves (but now discretized) for the limiting 0° and 30° incidence angles for each of the five species are also shown. The presence of Si is now more pronounced than in the DE data.

While the MTRX product was part of the design and implemented as an algorithm in the onboard digital processing unit of the instrument, a separation between ion species heavier than CNO was not envisaged in the original instrument design (Wilken et al., 1997). The SRIM curves shown in Figure 2 have been recalculated and updated after launch, using an updated version of the SRIM software.

As for the DE product, MTRX is an uncalibrated data product. For this reason, and due to the low time resolution, the MTRX data product was originally not considered to be very useful for science investigations. MTRX data was therefore originally not uploaded to the Cluster Science Archive.

A lesson learned from the Haaland et al. (2020) study was that for long-time studies addressing variations over solar cycles and for comparisons between large regions of space, the low time resolution and lack of directional information are less important. It was therefore decided to add MTRX data as a Cluster Science Archive RAPID product, and at the time of writing (early 2021), the ingestion of MTRX is ongoing. An

Table 1
Energy Thresholds for the 5 (Species) by 8 (Energy Channels) RMTRX product

	H	He	CNO	Si	Fe
1	74	101	243	401	709
2	86	137	408	648	1,080
3	104	166	515	818	1,344
4	130	206	611	934	1,524
5	174	266	743	1,082	1,689
6	253	362	929	1,272	1,817
7	423	535	1,203	1,520	1,961
8	718	817	1,526	1,854	2,126
Max	1,143	1,279	1,866	2,066	2,218

Numbers refer to the lower energy threshold in units of keV for a given species, and the last line shows the upper energy threshold for each of the 5 species: For example, energy channel 1 for Si covers the energy range between 401 and 648 keV; and Si channel 8 covers the energy range 1,854–2,066 keV.
Abbreviation: MTRX, matrix.

advantage of the MTRX data product is that all events are counted, there is no priority scheme to blur the relative intensities between the species or to distort the spectra.

In this paper, we will utilize a more compact representation of the data, RMTRX, where the 32 mass bins and 64 energy bins have been rebinned into a 5 × 8 matrix, with 5 mass bins (H, He, CNO, Si, Fe) and eight energy channels, which are now species dependent. Figure 2c shows how the 5 × 8 bins of RMTRX map to the 32 × 64 MTRX space. Note that the species channels have been expanded to fill any gaps between them, something most noticeable for oxygen. This allows for any spreading of the data beyond the expected range of incidence angles and for possible shifts downwards as the solid state detector efficiency degrades over time.

Energy thresholds for the five species and their eight energy channels of the RMTRX product are shown in Table 1. We primarily focus the spatial distribution and long term variations of Si ("Rock") and Fe ("Heavy Metal") from RMTRX, but we will also dwell on abundance ratios between species, e.g., [Si]/[O] and [Fe]/[O]. The energy binning allows us to create crude energy spectra (RMTRX data are uncalibrated, thus "crude") of Si and Fe. Due the prioritization scheme, this was not possible with the DE results reported in Haaland et al. (2020).

As in Haaland et al. (2020), we internally store the elements of the RMTRX in a table in a relational database. The time-stamp of each observation (i.e., center time of the 64 spin accumulation period) serves as a key to join the RAPID composition data with other tables, for example, spacecraft position, solar wind measurements as well as geomagnetic activity indices obtained from other data sources. Plots and statistics are constructed from pre-defined queries in this database. The use of a relational database makes it very simple to experiment with different thresholds (e.g., minimum and maximum count rates) or selection constraints (e.g., by only selecting observations by region or from certain solar activity ranges or geomagnetic activity levels).

3. Observations

Figure 3 shows an overview of RMTRX data coverage along with the F10.7 index, a proxy for solar activity. About 1.4 million records, corresponding to more than 25,000 h of RMTRX observations are available, most of them from SC2 and SC4. Recall that Cluster science operations started early 2001 and that data acquisition was limited in 2001 and 2002. Cluster is still in operation, and MTRX data are still collected by SC2 and

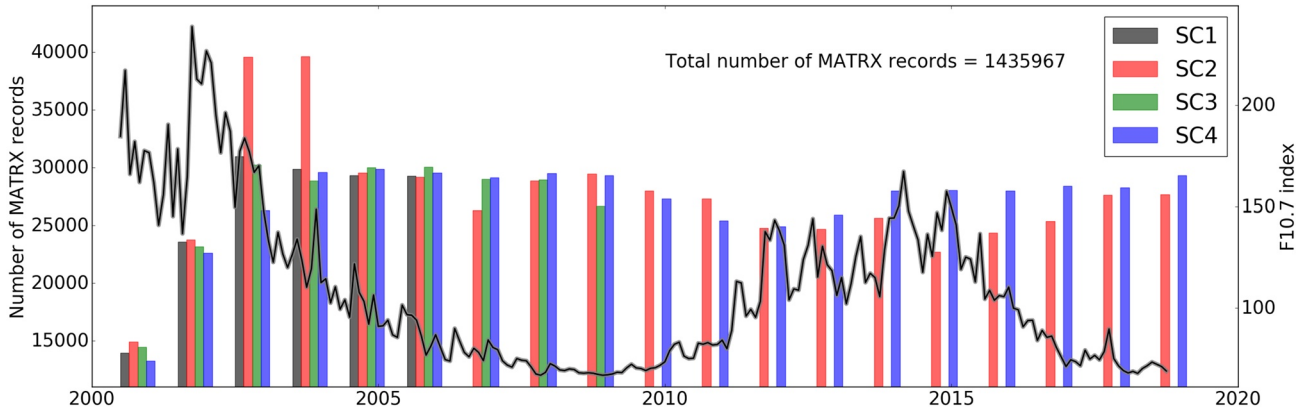

Figure 3. Overview of RMTRX data coverage (number of MTRX records) from each of the four Cluster spacecraft. The black curve overlaid shows monthly averages of F10.7 index, a proxy for solar activity. MTRX, matrix.

SC4, but RAPID IIMS measurements are only available until early 2007 for SC1 and early 2009 for SC3. As we shall see later, Si and Fe are only observed during a fraction of the total observation time.

Observation time for a given region is not necessarily identical to the Cluster dwell time in that region. Since July 2010, RAPID IIMS has been switched off during radiation belt passages. This measure is taken to preserve the micro channel plates in the start/stop system during times of high radiation. RAPID measurements are also suspended during scheduled spacecraft maneuvers and eclipses. In addition, there are occasional instrument reboots and system down-times. As seen from Figure 3, observations were also limited due to limited data acquisition the first few years of Cluster operations.

The central IIMS head (Sensor 2 in Figure 1) severely deteriorated on all four spacecraft over the first months of operation, presumably due to sunlight leakage and subsequent photoelectron emissions and saturation of the microchannel plates providing the start/stop signals. MTRX or RMTRX do not contain directional information, but this damage obviously leads to overall lower count rates than would have been possible with all three IIMS sensor heads fully operational.

3.1. Estimating Fe and Si Abundance

Since the MTRX data are uncalibrated, we are not able to present calibrated fluxes. Instead, we use *occurrence rate* and *intensity* to characterize and show how Si and Fe abundance varies spatially by plasma region and temporally due to variations in solar irradiance and geomagnetic activity.

Occurrence rate is calculated the same way as in Haaland et al. (2020) and is defined as the percentage of observation time in which Si or Fe count rates above a certain level are observed. This minimum count threshold has been introduced to avoid classifying random single counts as valid Si or Fe detections (a typical scenario is that a particle hits the start foil and shortly thereafter *another* particle hits the energy detector, thus generating what *appears* to be a valid E-TOF event). In the present study, we require 10 or more counts per record (64 spins $\simeq$ 4 min, see below) within the E-TOF range corresponding to Si in order to classify it as a valid and unambiguous Si detection. The same threshold is also applied to Fe counts. There is no way to distinguish *apparent* events from valid E-TOF events, and we will discuss consequences of raising or lowering the minimum threshold in Section 3.2.2 below.

Intensity is defined as the number of counts per second divided by the energy range and have units of $[s^{-1}\ keV^{-1}]$. With eight energy ranges (see Table 1), we have eight intensities for each species, and this allows us to construct intensity versus energy spectra for both Si and Fe. For each energy range, we average (using the mean moment) over a number of records with valid counts (count rates above threshold) within a spatial region or over a time interval. Both Si and Fe are rare species in geospace, and as we shall see later, the typical situation is that a single MTRX record contains no Si or Fe counts above the minimum threshold. Consequently, both mode and median of the full distribution are typically zero, so the mean is the only sensible statistical moment to characterize Si and Fe intensities.

3.2. Fe and Si Abundance and Characteristics by Region

We now investigate how Si and Fe are distributed across the regions of space traversed by Cluster over the last 19 years. As in Christon et al. (2017) and Haaland et al. (2020), we define regions and plasma regimes in space by spacecraft location rather than local plasma properties.

3.2.1. Definition of "Region"

Table 2 shows the definition of the regions and Figure 4 shows spectra of Si and Fe as well as the locations of individual measurements for each of these regions.

Within the magnetosphere (inner magnetosphere, plasma sheet, lobe, and high-latitude polar cap and cusps) regions are all defined by their Geocentric Solar Magnetic (GSM) coordinates. Observations in the solar wind region are taken outside the model magnetopause, the static, parabolic model by Fairfield (1971), with a magnetopause standoff distance of 13 Re. Most of the measurements outside the magnetosphere are actually from the magnetosheath, that is, a plasma regime consisting of braked and thermalized solar wind plasma. With its approximately 20 Earth radii (Re) apogee, Cluster also regularly crosses the upstream bow

Table 2
Summary of Cluster RAPID Si and Fe Observations and Their Occurrence Rates by Region (Top five rows)

		Observation	Si occurrence	Fe occurrence
Region	Definition of region	Time [h]	[% of time]	[% of time]
Solar wind and Magnetosheath	Outside static model by Fairfield (1971)	32,654	3.8	1.5
High latitudes, polar cap and cusp	Poleward of 60° Latitude	8,931	2.6	1.1
Lobe	$X_{GSM} \leq -5$ Re	18,203	2.3	1.0
	$\lvert Y\rvert_{GSM} \leq 15$Re			
	$\lvert Z\rvert_{GSM} \geq 4$ Re			
Plasma sheet	$X_{GSM} \leq -5$ Re	10,906	19.5	10.0
	$\lvert Y\rvert_{GSM} \leq 15$Re			
	$\lvert Z\rvert_{GSM} \leq 4$ Re			
Inner magnetosphere	Cluster inside 6.6Re radial distance	8,635	$42.8^{(*)}$	36.0
Entire Cluster coverage	Total observation time 2001–2019	100,730	10.4	6.4

The bottom row shows the sum over all regions. Observation time shown in the third column is the total number of accumulated hours of RMTRX measurements from all spacecraft in that region. Occurrence rates for Si and Fe are percentages of observation time where count rates are above our noise threshold. Definition of regions is identical to Haaland et al. (2020). (*) See notes about the possible presence of molecular ions in Section 3.2.3.

Abbreviations: Fe, Iron; Si, silicon; RAPID, Research with Adaptive Particle Imaging Detectors.

shock and enters the pristine solar wind during the season February to April. Compositionwise, we do not expect any differences between the pristine solar wind or magnetosheath, so we have not distinguished between these regions.

With a time resolution of 64 spins and a spin period of slightly more than 4 s, the time resolution of the MTRX data is approximately 250 s, so we have to use a very conservative approach to define plasma regimes and regions. Cluster moves with several km/s, relative to a fixed (GSE or GSM) coordinate system, so the spatial resolution is at best of the order of 1,000 km. Boundaries in space, for example, the tail plasma sheet, bow shock or magnetopause can move with velocities of 100's of km/s (e.g., Lepidi et al., 1996; Paschmann et al., 2018; Sergeev et al., 2003) over distances of several Re. We are therefore not able to calculate any gradients in the measurements inside regions or across boundaries.

The orbit of Cluster changes over time so there will be some bias in the sampling of the various regions. Early in the mission apogee was close to the ecliptic plane with roughly equal sampling in the northern and southern hemisphere (Z_{GSE} ranges). With time (and changing solar activity), apogee shifted below the ecliptic plane, resulting in more sampling in the (southern hemisphere) tail lobes, where plasma densities and particle fluxes are usually lower than other regions of geospace. Recall also that RAPID IIMS is shut down inside the radiation belts after 2010.

3.2.2. Si and Fe Occurence Rate by Region

From Table 2, it becomes clear that Si and Fe in the energy ranges discussed here are rare species. Occurrence rates do not exceed 50% in any of the regions and from the last row in Table 2, we can infer that over all regions, only about 10% of the MTRX records contain traces of Si, and only 6% contain traces of Fe. The likelihood of detecting Si and/or Fe is smallest in the low density polar cap and lobe regions, where Si is observed in less than 3% of the observation time, and Fe only observed around 1% of the observation time.

To investigate how robust these results are, we re-ran the queries with several minimum count thresholds and also adjusted the boundaries of our regions. If we lower the minimum count threshold from 10 counts per record to five counts per record (akin to lowering the "noise" threshold), the occurrence rates in the different regions increase by up to a factor 2, but the relative differences between the different regions remain almost the same. Adjusting the location and extent of the regions has a much smaller effect. If we move e.g., the "Solar wind" region 2 Re further out (i.e., setting the magnetopause standoff distance to 15 Re instead of 13 Re in the Fairfield (1971) magnetopause model), the Si occurrence rate only dropped 0.4%.

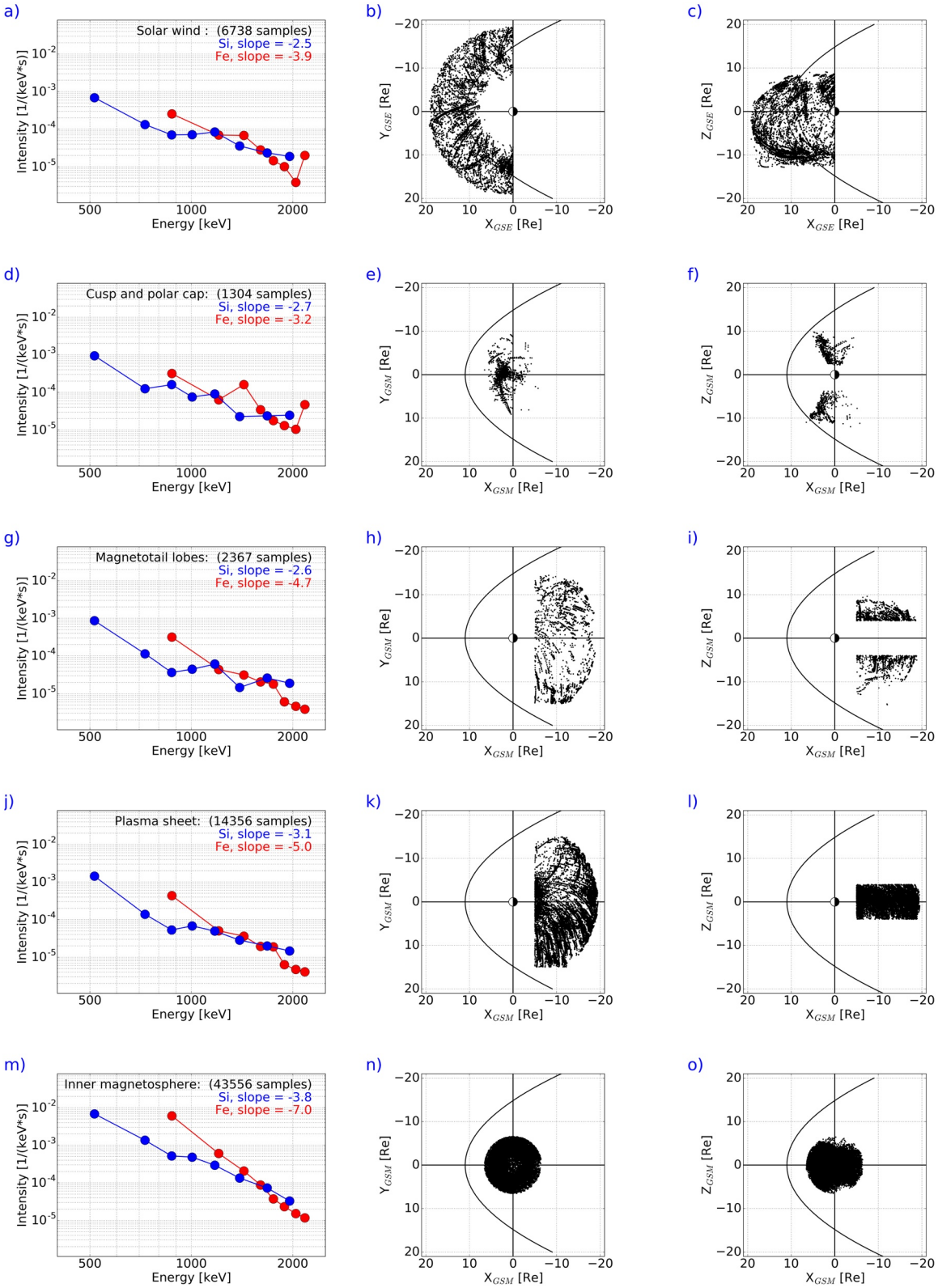
a)
Solar wind : (6738 samples)
Si, slope = -2.5
Fe, slope = -3.9
b)
c)
d)
Cusp and polar cap: (1304 samples)
Si, slope = -2.7
Fe, slope = -3.2
e)
f)
g)
Magnetotail lobes: (2367 samples)
Si, slope = -2.6
Fe, slope = -4.7
h)
i)
j)
Plasma sheet: (14356 samples)
Si, slope = -3.1
Fe, slope = -5.0
k)
l)
m)
Inner magnetosphere: (43556 samples)
Si, slope = -3.8
Fe, slope = -7.0
n)
o)
Intensity [1/(keV*s)]
Energy [keV]
Y_{GSE} [Re]
X_{GSE} [Re]
Z_{GSE} [Re]
Y_{GSM} [Re]
X_{GSM} [Re]
Z_{GSM} [Re]

3.2.3. Si and Fe Intensities and Spectra by Region

The division into eight energy channels allows us to study the energy distribution of the observed Si and Fe ions. With energy thresholds of several 100 keVs for both Si and Fe, we obviously only get a part of the energy spectrum. The left column of Figure 4 shows energy spectra for the five regions of space investigated, and list the number of samples and the spectral slope, calculated as the best straight line fit, for each spectrum. We note that the slopes are generally steeper (larger negative slope numbers) for Si than for Fe. Consequently, in the energy range 700–2,000 keV, where we have measurements of both species, Fe intensities are generally higher than those of Si. There are large statistical variations (not indicated) in the measurements.

Figure 4 shows that average intensities vary between regions, but the energy spectra from the different regions are overall very similar. One interpretation of this is that most of the Si and Fe are of the the same origin, most likely the solar wind. In the inner magnetosphere, and in particular during disturbed conditions, some of the Si counts may be due to ionospheric material, such as molecular N_2, NO and O_2, which have masses similar to that of silicon. The measured energies are a combination of bulk energy (e.g., due to high flow velocities) and thermal velocity (gyration around magnetic field lines). The lack of directional information in MTRX measurements means that we cannot distinguish between these two contributions.

Solar wind. The solar wind is also the region where average flow velocities are highest; the solar wind bulk velocity typically varies between 300 – 1,000 km/s at 1 AU, but more extreme values can occur (Feldman et al., 2005). For Si this corresponds to flow energies of up to 150 keV. For Fe, with its higher mass, solar wind bulk velocities correspond to bulk energies up to 300 keV. Additional acceleration can take place due to processes in the solar wind, such as e.g., reconnection (e.g., Phan et al., 2006, 2020) or accelerations at shock fronts embedded in the solar wind (e.g., Prinsloo et al., 2019; Zank et al., 2007). It is therefore not surprising that Si and Fe of high energies are observed in this region.

As noted in the introduction, there has been more focus on composition measurements in the solar wind compared to the magnetosphere, so for the solar wind, we have references values for abundances and abundance ratios. Reames et al. (1994); Aellig et al. (1999), and Bochsler (2007) compared relative abundances between various species in the solar wind, and from their [Si]/[O] and [Fe]/[O] ratios, a [Fe]/[Si] ratio in the range 1–10 can be inferred. This value is roughly consistent with our result for the lowest energy range.

Polar cap, cusp and lobe regions. Panels (d) and (g) in Figure 4 show the energy spectra in the polar cap and the magnetically connected tail lobe regions. Locations of individual observations are shown in panels (e) to (f) and (h) to (i), respectively. In terms of volume, the cusp region is the smallest region considered, and also has the lowest number of observed Fe and Si events. The lobes encompass a much larger volume, but occurrence rates for both Si and Fe are lower than the in the other regions (see Table 2).

Escape of atmospheric material, both neutrals (e.g., Moore & Horwitz, 2007) and ions (ion outflow, see e.g., Yau & Andre, 1997) from the high latitude atmosphere has been established as an important process for the loss of atmospheric material and filling of the magnetotail lobes. Transport is through the cusp and polar cap along (convecting) magnetic field lines threading the lobes. Both Si and Fe exist in the Earth's atmosphere (e.g., von Zahn et al., 2002; Plane et al., 2015), primarily due to meteor ablation in the mesosphere (Kane & Gardner, 1993), and concentrations are much higher than in the solar wind. As shown in the recent paper by Christon et al. (2017), heavy ions can also escape into the magnetosphere.

It would perhaps be natural to associate Si and Fe in the polar cap and lobe regions with such outflow processes. However, plasma of atmospheric (ionospheric) origin is usually very cold (low thermal energies), and no known acceleration mechanisms able to energize Si and Fe ions to 100s of keV exist in these regions. Escape mechanisms and transport paths of heavy ions are also still poorly understood.

Figure 4. Spectra of Si and Fe based on Cluster RAPID RMTRX observations from five different key regions in geospace. The leftmost panel in each row shows the derived energy spectra for Si (blue) and Fe (red). Spectral slopes and number of observations (≃4 min averages) are indicated in the upper right of these panels. The second and third column shows projections of the location in space of records where both Fe and Si were observed. From top to bottom, the figure shows spectra and locations for: (a)–(c) the solar wind and magnetosheath region; (d)–(f) the polar caps and cusps; (g)–(i) the magnetotail lobes; (j)–(l) the tail plasma sheet; (m)–(o) the inner magnetosphere. See Section 2 for definitions of these regions and a summary of their Si and Fe abundance. MTRX, matrix; RAPID, Research with Adaptive Particle Imaging Detectors.

In the cusp, strong local accelerations mechanisms exists (e.g., Chen et al., 1998; Fritz, 2001). While most of the particles in the cusp region are probably of magnetosheath origin, there are also observations (e.g., Kremser et al., 1995; Trattner et al., 2001) suggesting that the cusp contains ions of magnetospheric origin.

Plasma sheet and inner magnetosphere. Within the Earth's magnetosphere, there are few regions where processes able to accelerate heavy ions up to the ≥400 keV energies of the MTRX data can occur. In the plasma sheet, magnetic reconnection can create jetting with bulk velocities up to and sometimes above 1,000 km/s (bursty bulk flows, see e.g., Angelopoulos et al., 1992; Baumjohann et al., 1990). Bulk velocities in this range correspond to flow energies of approximately 150 keV for Si and approximately 300 keV for Fe. Thus, while tail reconnection may be able to provide significant bulk acceleration, this is not enough to explain the energy spectra in Figure 4j.

Particle acceleration can also take place in the inner magnetosphere and during transport from the distant tail to the near-Earth tail. Acceleration mechanisms include direct accelerations by electric fields, betatron or Fermi acceleration associated with dipolarization of the magnetic field, as well as wave-particle interactions (a good overview of various acceleration processes in the magnetotail can be found in e.g., Birn et al., 2012). Combined, these mechanisms can accelerate ions (and electrons) to very high energies (up to MeV) as evident in, for example, the radiation belts.

As explained in Section 2.1, no charge state information is available from RAPID. Ions of solar wind origin are usually associated with high charge states. Although some charge exchange takes place, primarily through interaction with neutral hydrogen atoms in the Earth's geocorona, it is reasonable to assume that the observed Si and Fe ions still retain rather high charge states as they get transported across the bow shock and magnetopasue into the magnetosphere. Consequently, they should be accelerated more effectively than single charged particles of the same species (e.g., Bingham et al., 2020).

Given that the measurements presented here are taken over a time period of 19 years, with no regards to solar activity level or geomagnetic activity (this is addressed in the next section), there is significant statistical spread in the data. For both Si and Fe, the measurement standard deviation in each energy range is often comparable to or larger than the mean (we have therefore not added error bars indicating any statistical spread, they would fill the vertical scale). Still, from Figure 4, one can infer a spectral change across regions: The slopes for both Si and Fe are steeper in the plasma sheet and inner magnetosphere than the other regions. This may be an indication of additional acceleration, most effective in the lower energy range of MTRX measurements, in the plasma sheet and inner magnetosphere. For the Si curve, another possible explanation is the additional presence of ionospheric molecules as reported by, for example, Klecker et al. (1986) and Seki et al. (2019).

4. Time Variations in Fe and Si Occurrence

At the time of writing, Cluster has been in space for more than 20 years. RAPID MTRX observations are so far available from 19 years of science operations. Such long term observation series allow us to assess the role of solar variability, of which the 11 years solar cycle is the most pronounced and geomagnetic activity in response to geomagnetic storms.

4.1. Si and Fe Abundance as Function of Solar Variability

Long-term variability in the Si and Fe abundances can be inferred from Figure 5a, which shows histograms with the numbers of MTRX samples from SC2 and SC4 containing Si and Fe observations during the 19 years of science operations. Overplotted as a solid line is the F10.7 index, a proxy for solar activity (e.g., Covington, 1969; Schonfeld et al., 2015). Solar maximum during solar cycle 23 was around 2001–2002, with the minimum around 2008–2009 marking the start of solar cycle 24.

Both Fe and Si occurrence rates follow the solar cycle variation, albeit somewhat shifted in time. The highest occurrence rates and intensities are observed around the waning phase of solar cycle 23. Similarly, the lowest occurrence rates are observed around 2010–2011, a few years after the 2008–2009 solar minimum. Solar cycle 24 was less active (manifested by fewer active sunspots, and lower geomagnetic activity), and reached maximum around 2014. Si and Fe occurrence rates and intensities seem to follow the solar activity also for

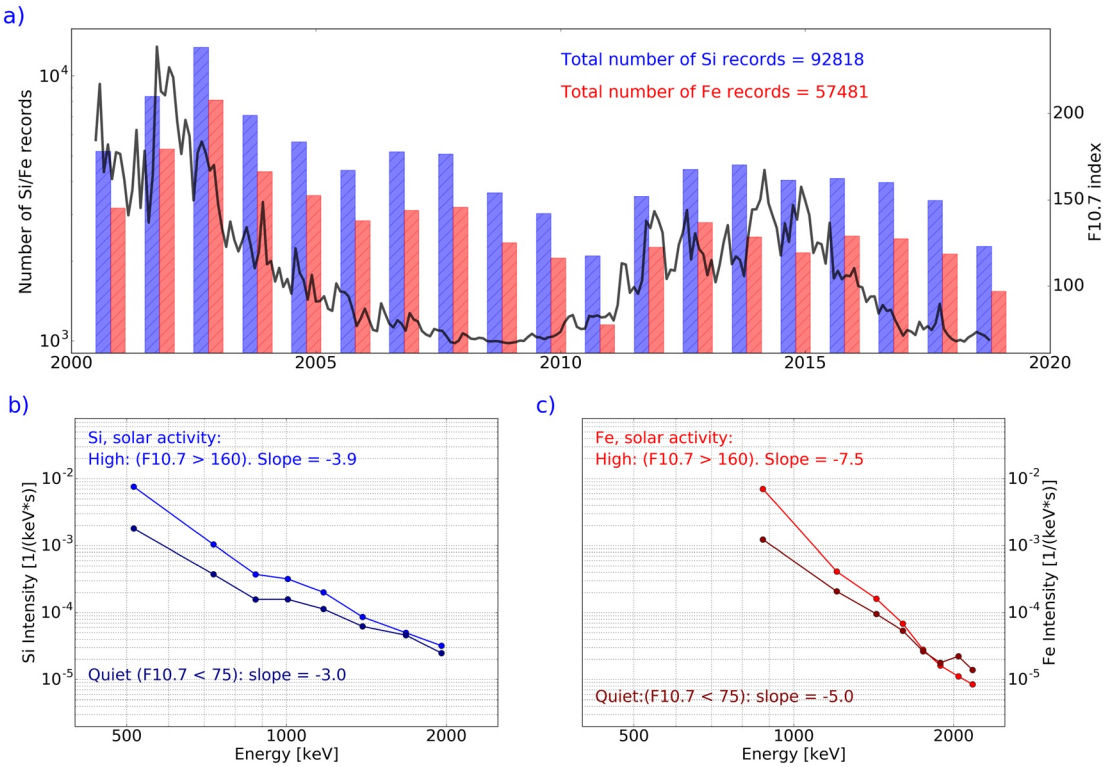

Figure 5. Panel (a): Histogram of Si and Fe abundance (i.e., number of observations above noise threshold from SC2 and SC4) during 2001–2019, with the F10.7 solar irradiation proxy overplotted as a black line. Panels (b) and (c) show energy spectra for Si and Fe, respectively for low (F10.7 < 75) and high (F10.7 > 160) solar activity. A clear correlation between solar activity and occurrence rate and intensities can be inferred.

this period. Note that the orbital bias discussed in Section 3.2, as well as possible sensor degradations can also affect the absolute number of Si and Fe counts.

Panels (b) and (c) show energy spectra similar to those in Figure 4, but now for two different solar activity levels. "High" solar activity are measurements sampled when the F10.7 index was 160 or above. This subset contains approximately 15% of the all records with Fe and Si observations above the minimum count threshold. The subset for "low" solar activity only contains (also around 15% of samples) measurements sampled when the F10.7 index was below 75.

In panel (b), the upper blue curve shows Si for "high" solar activity subset, and lower dark blue curve shows the corresponding spectrum for "low" solar activity. Panel (c) shows the corresponding spectra for Fe. We note a clear response in the spectra to solar activity. High solar activity is associated with higher Si and Fe intensities and a steeper slope. We do not show spectra for intermediate solar activity, but as expected, they fall between the "high" and "low" curves for both Si and Fe.

4.2. Si and Fe Abundance as Function of Geomagnetic Activity

Figure 6a shows the same Si and Fe occurrence statistics histogram as in Figure 5a, but now with minimum (i.e., most disturbed) monthly Dst (e.g., Bergin et al., 2020; Sugiura, 1964) overplotted. Dst is a measure of ground based magnetic perturbations caused by the enhanced energy in the ring current. Negative Dst deflections indicate a stronger ring current, typically caused by enhanced solar wind - magnetosphere energy transfer over a period of several days during geomagnetic storms.

Once again, we note a correlation between the curves, albeit not as pronounced as for solar activity. Higher occurrence rates of Si and Fe are observed during the period 2001–2005, corresponding to a period of enhanced geomagnetic activity, manifested as more frequent and larger negative Dst deflections. Due to the very low Si and Fe count rates we are not able to investigate the role of individual geomagnetic storms

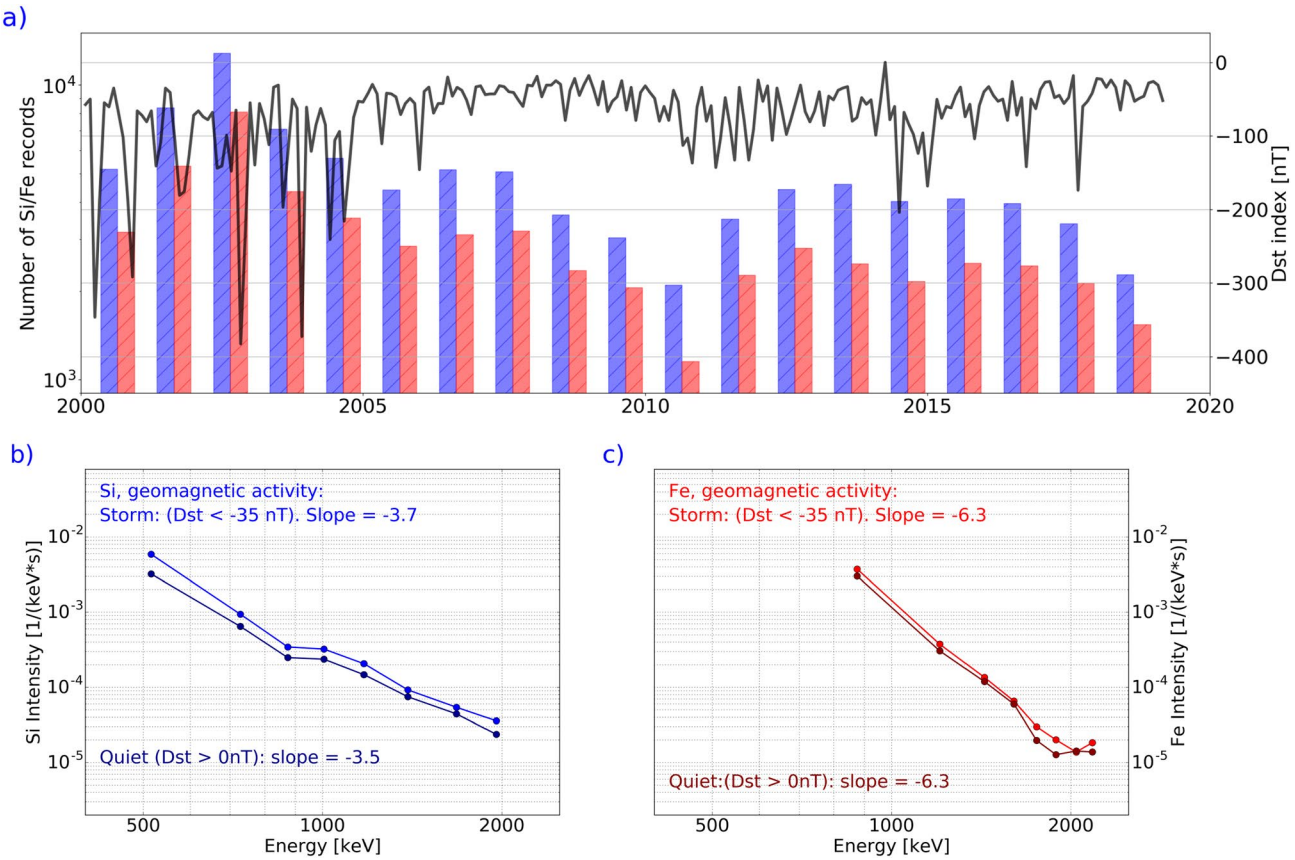

Figure 6. Similar to Figure 5, but with responses to geomagnetic activity. Panel (a): Si and Fe abundance as histograms with the minimum Dst, a proxy for geomagnetic activity overplotted as a black line. Panel (b) and (c): Energy spectra for Si and Fe for high (Dst values below −35 nT) and low (positive Dst values) geomagnetic activity. Fe, iron; Si, silicon.

or transient geoactivity leading to enhanced acceleration processes inside the magnetosphere. Most likely, the correlation between Dst and Si and Fe occurrence rates is a result of the general relationship between geomagnetic activity and solar activity (e.g., Echer et al., 2004; D. T. Young et al., 1982).

Panels (b) and (c) of Figure 6 show energy spectra for Si and Fe for quiet and active conditions. Here, "quiet" is defined as any period with zero or positive Dst values, and may encompass observation taken during storm sudden commencements, often associated with a compression of the magnetosphere (e.g., Araki, 1994). "Storm" is defined as any period with Dst values below −35 nT. This value is somewhat arbitrary but gives us approximately the 15% of samples with strongest geomagnetic activity.

Unlike the response to solar activity, there is almost no difference between the spectra for "quiet" and "storm" periods. Thus, any enhanced acceleration mechanisms operating during stormtime conditions (e.g., stronger and/or more frequent bursty bulk flow activity and reconnection in the tail and substorm injections) do not seem to energize Fe or Si or alter the energy spectra significantly, at least not within the energy range covered by the MTRX measurements.

5. Summary

We have used a combination of E-TOF measurements from the RAPID instrument onboard the Cluster satellites to study energetic ions with masses corresponding to that of Si and Fe. Each individual measurement (sample) is based on accumulation of individual E-TOF events over a period of 64 spins (ca 4 min). The RAPID ion detector is sensible to Si in the energy ranges 400–2,100 keV, and Fe in the energy range 700–2,200 keV. No charge state separation is possible, and no directional information can be derived from these measurements.

Over the period 2001–2019 covered by this study, more than 1.4 million samples, corresponding to 25,000 h of observations were collected, and the *occurrence rate* and *intensity* of Si and Fe were investigated. Si and Fe are both rare species in geospace, and *occurrence rate* in this context means the probability of detecting any Si or Fe at all within a collection of samples accumulated either inside a region or within disturbance parameter ranges. *Intensity* is defined as the average number of Si or Fe counts within a certain time interval and over a certain energy range.

The result of this study can be summarized as follows:

- Both Si and Fe are rare species but were detected in traceable quantities in all regions of geospace traversed by Cluster
- The highest occurrence rates were found in the inner magnetosphere where also particle fluxes of lighter ions are highest. In the inner magnetosphere, about 36% of all samples contained Fe and 43% of the samples contained Si (with the provision that some of the Si counts may be from molecular ions of ionospheric origin with similar atomic mass)
- The lowest occurrence rates were found in the magnetotail lobes. Si was found in only about 2% of observations in this region, and Fe was found in about 1% of the lobe samples
- Energy spectra for both Si and Fe are very similar in all regions of space probed, suggesting a common source and very little local acceleration/energization
- The energy spectra is steeper for Fe than Si in all regions
- Occurrence rates are modulated by solar activity; The probability of observing Si and Fe increases during periods with high solar activity (near solar maximums)
- Intensities are also modulated by solar activity: Average intensities are higher during active solar periods for both Si and Fe
- We find little or no response to geomagnetic activity in the occurrence rates or intensities of both Si and Fe

While the measurements presented here provide some information about the distribution and long term variations of Si and Fe ions in geospace, they also leave us with some open questions that an instrument like RAPID cannot answer:

- What are the charge states of the observed Si and Fe ions?
- How does the charge state change due to charge exchange processes during transport across boundaries and through the various regions of geospace?
- What about lower energies; Can low energy Si and Fe from, for example, space debris fragmentation in the atmosphere escape and "contaminate" the magnetosphere?
- What is the composition of our magnetosphere, and what are the relative contributions of heavy atoms from the solar wind and ionosphere?

The last question is rather fundamental and also encompasses other ion species. Whereas the solar wind source of minor ions is fairly well mapped, less is known about the terrestrial outflow of heavy ions, neither in terms of composition, forces responsible for outflow, or transport paths. Somewhat surprisingly, we are in a situation where we know more about the composition of the magnetospheres of some of our neighbor planets than our own Earth. A better understanding of the magnetospheric composition may be achieved by coordinated efforts to better explore and utilize all existing observations. Still, limitations in instrument precision and mass resolution in existing data makes a full mapping of the composition difficult. A dedicated geospace composition mission would probably be the only option to address all the above questions.

Data Availability Statement

All the Cluster data, including the MTRX and RMTRX data products from RAPID, are available from the Cluster Science Archive: https://www.cosmos.esa.int/web/csa. The data format as well as comprehensive information about the RAPID instrument are described in Daly and Kronberg (2020) and Kronberg et al. (2020).

OMNI data used to check correlations with geomagnetic activity (Dst/SYM-H) and solar illumination (F10.7) are available from the NASA Coordinated Data Analysis Web (CDAWeb): https://cdaweb.gsfc.nasa.gov/index.html.

Acknowledgments
Cluster RAPID was supported by the European Space Agency through the Cluster Science Archive activities and by the Deutsches Zentrum für Luft- und Raumfahrt (DLR) under grant 50 OC 1602.

References

Aellig, M. R., Hefti, S., Grünwaldt, H., Bochsler, P., Wurz, P., Ipavich, F. M., & Hovestadt, D. (1999). The Fe/O elemental abundance ratio in the solar wind as observed with SOHO CELIAS CTOF. *Journal of Geophysical Research*, *104*(A11), 24769–24780. https://doi.org/10.1029/1999JA900309

Aikin, A. C., & Goldberg, R. A. (1973). Metallic ions in the equatorial ionosphere. *Journal of Geophysical Research*, *78*(4), 734. https://doi.org/10.1029/JA078i004p00734

Angelopoulos, V., Baumjohann, W., Kennel, C. F., Coronti, F. V., Kivelson, M. G., Pellat, R., et al. (1992). Bursty bulk flows in the inner central plasma sheet. *Journal of Geophysical Research*, *97*(A4), 4027–4039. https://doi.org/10.1029/91JA02701

Araki, T. (1994). A physical model of the geomagnetic sudden commencement. In Solar Wind Sources of Ultra low frequence magnetospheric Waves (Vol. 81). AGU.

Baumjohann, W., Paschmann, G., & Luehr, H. (1990). Characteristics of high-speed ion flows in the plasma sheet. *Journal of Geophysical Research*, *95*(A4), 3801–3809. https://doi.org/10.1029/JA095iA04p03801

Bergin, A., Chapman, S. C., & Gjerloev, J. W. (2020). AE, D_{ST}, and their SuperMAG counterparts: The effect of improved spatial resolution in geomagnetic indices. *Journal of Geophysical Research*, *125*(5). e2020JA027828. https://doi.org/10.1029/2020JA027828

Bilitza, D., Altadill, D., Truhlik, V., Shubin, V., Galkin, I., Reinisch, B., & Huang, X. (2017). International reference ionosphere 2016: From ionospheric climate to real-time weather predictions. *Space Weather*, *15*(2), 418–429. https://doi.org/10.1002/2016SW001593

Bingham, S. T., Cohen, I. J., Mauk, B. H., Turner, D. L., Mitchell, D. G., Vines, S. K., et al. (2020). Charge-state-dependent energization of suprathermal ions during substorm injections observed by mms in the magnetotail. *Journal of Geophysical Research*. *125*(10), e2020JA028144. https://doi.org/10.1029/2020JA028144

Birn, J., Artemyev, A. V., Baker, D. N., Echim, M., Hoshino, M., & Zelenyi, L. M. (2012). Particle acceleration in the magnetotail and aurora. *Space Science Reviews*, *173*(1–4), 49–102. https://doi.org/10.1007/s11214-012-9874-4

Bochsler, P. (2007). Minor ions in the solar wind. *The Astronomy and Astrophysics Review*, *14*(1), 1–40. https://doi.org/10.1007/s00159-006-0002-x

Brownlee, D. E., Tsou, P., Anderson, J. D., Hanner, M. S., Newburn, R. L., Sekanina, Z., et al. (2003). Stardust: Comet and interstellar dust sample return mission. *Journal of Geophysical Research*, *108*(E10), 8111. https://doi.org/10.1029/2003JE002087

Campbell-Brown, M. D. (2019). Meteoroid structure and fragmentation. *Planetary and Space Science*, *169*, 1–7. https://doi.org/10.1016/j.pss.2019.03.005

Chappell, C. R., Moore, T. E., & Waite, J. H. Jr. (1987). The ionosphere as a fully adequate source of plasma for the Earth's magnetosphere. *Journal of Geophysical Research*, *92*(A6), 5896–5910. https://doi.org/10.1029/JA092iA06p05896

Chen, J., Fritz, T. A., Sheldon, R. B., Spence, H. E., Spjeldvik, W. N., Fennell, J. F., et al. (1998). Cusp energetic particle events: Implications for a major acceleration region of the magnetosphere. *Journal of Geophysical Research*, *103*(A1), 69–78. https://doi.org/10.1029/97JA02246

Christon, S. P., Gloeckler, G., Williams, D. J., Mukai, T., McEntire, R. W., Jacquey, C., et al. (1994). Energetic atomic and molecular ions of ionospheric origin observed in distant magnetotail flow-reversal events. *Geophysical Research Letters*., *21*(25), 3023–3026. https://doi.org/10.1029/94GL02095

Christon, S. P., Hamilton, D. C., Plane, J. M. C., Mitchell, D. G., Grebowsky, J. M., Spjeldvik, W. N., & Nylund, S. R. (2017). Discovery of suprathermal ionospheric origin Fe^{+} in and near earth's magnetosphere. *Journal of Geophysical Research*, *22*. https://doi.org/10.1002/2017JA024414

Covington, A. E. (1969). Solar radio emission at 10.7 cm, 1947–1968. *Journal of the Royal Astronomical Society of Canada*, *63*, 125.

Cowley, S. W. (1985). Cometary science: ICE encounters giacobini-zinner. *Nature*, *317*(6036), 381. https://doi.org/10.1038/317381a0

Daly, P. W., & Kronberg, E. (2020). *User guide to the RAPID measurements in the Cluster Science Archive (CSA), technical report*. European Space Agency.

Dandouras, I. (2020). Molecular ions in the terrestrial magnetosphere. *Nature*.

Eberhardt, P., Geiss, J., Graf, H., Grögler, N., Mendia, M. D., Mörgeli, M., et al. (1972). Trapped solar wind noble gases in Apollo 12 lunar fines 12001 and Apollo 11 breccia 10046. *Lunar and Planetary Science Conference Proceedings*, *3*, 1821–1856.

Echer, E., Gonzalez, W. D., Gonzalez, A. L. C., Prestes, A., Vieira, L. E. A., dal Lago, A., et al. (2004). Long-term correlation between solar and geomagnetic activity. *Journal of Atmospheric and Solar-Terrestrial Physics*, *66*(12), 1019–1025. https://doi.org/10.1016/j.jastp.2004.03.011

ESA. (2020). *Space sustainability: The economics of space debris in perspective*. OECD.

Fairfield, D. H. (1971). Average and unusual locations of the Earth's magnetopause and bow shock. *Journal of Geophysical Research*, *76*(28), 6700. https://doi.org/10.1029/JA076i028p06700

Feldman, U., Landi, E., & Schwadron, N. A. (2005). On the sources of fast and slow solar wind. *Journal of Geophysical Research*, *110*(A7), A07109. https://doi.org/10.1029/2004JA010918

Fomenkova, M. N., Evlanov, E. N., Muknin, L. M., Prilutski, O. F., Sagdeev, R. Z., & Zubkov, B. V. (1989). Chemical composition and properties of comet Halley dust particles as obtained during VEGA mission. *Meteoritics*, *24*, 267.

Fritz, T. A. (2001). The cusp as a source of magnetospheric energetic particles, currents, and electric fields: A new paradigm. *Space Science Reviews*, *95*(1), 469–488. https://doi.org/10.1023/A:1005286908441

Fritz, T. A., Zurbuchen, T. H., Gloeckler, G., Hefti, S., & Chen, J. (2003). The use of iron charge state changes as a tracer for solar wind entry and energization within the magnetosphere. *Annales Geophysicae*, *21*(11), 2155–2164. https://doi.org/10.5194/angeo-21-2155-2003

Geiss, J., Eberhardt, P., Bühler, F., Meister, J., & Signer, P. (1970). Apollo 11 and 12 solar wind composition experiments: Fluxes of He and Ne isotopes. *Journal of Geophysical Research*, *75*(31), 5972. https://doi.org/10.1029/JA075i031p05972

Geiss, J., Gloeckler, G., Balsiger, H., Fisk, L. A., Galvin, A. B., Gliem, F., et al. (1992). Plasma Composition in jupiter's magnetosphere: Initial results from the solar wind ion composition spectrometer. *Science*, *257*(5076), 1535–1539. https://doi.org/10.1126/science.257.5076.1535

Geiss, J., Gloeckler, G., & von Steiger, R. (1995). Origin of the solar wind from composition data. *Space Science Reviews*, *72*(1–2), 49–60. https://doi.org/10.1007/BF00768753

Gilbert, J. A., Lepri, S. T., Landi, E., & Zurbuchen, T. H. (2012). First measurements of the complete heavy-ion charge state distributions of C, O, and Fe associated with interplanetary coronal mass ejections. *The Astrophysical Journal*, *751*(1), 20. https://doi.org/10.1088/0004-637x/751/1/20

Gloeckler, G., Geiss, J., Balsiger, H., Bedini, P., Cain, J. C., Fischer, J., et al. (1992). The solar wind ion composition spectrometer. *Astronomy & Astrophysics Supplement Series*, *92*(2), 267–289.

Grande, M., Perry, C. H., Blake, J. B., Chen, M. W., Fennell, J. F., & Wilken, B. (1996). Observations of iron, silicon, and other heavy ions in the geostationary altitude region during late March 1991. *Journal of Geophysical Research*, *101*(A11), 24707–24718. https://doi.org/10.1029/96JA00044

Gulkis, S., & Alexander, C. (2008). Composition measurements of a comet from the Rosetta orbiter spacecraft. *Space Science Reviews*, *138*(1–4), 259–274. https://doi.org/10.1007/s11214-008-9335-2

Haaland, S., Daly, P. W., Vilenius, E., Krcelic, P., & Dandouras, I. (2020). Suprathermal Fe in the earth's plasma environment: Cluster RAPID observations. *Journal of Geophysical Research*, *125*(2), e2019JA27596. https://doi.org/10.1029/2019JA027596

Heritier, K. L., Altwegg, K., Balsiger, H., Berthelier, J. J., Beth, A., Bieler, A., et al. (2017). Ion composition at comet 67P near perihelion: Rosetta observations and model-based interpretation. *Monthly Notices of the Royal Astronomical Society*, *469*, S427–S442. https://doi.org/10.1093/mnras/stx1912

Hollingsworth, A., Engelen, R. J., Textor, C., Benedetti, A., Boucher, O., Chevallier, F., et al. (2008). Toward a monitoring and forecasting system for atmospheric composition: The GEMS project. *Bulletin of the American Meteorological Society*, *89*(8), 1147. https://doi.org/10.1175/2008BAMS2355.1

Huber, M. C. E., Pauluhn, A., & Timothy, J. G. (2010). *Observing photons in space*. ESA Publications Division (ISBN: 978-92-92221-938-3).

Inness, A., Ades, M., Agustí-Panareda, A., Barré, J., Benedictow, A., Blechschmidt, A.-M., et al. (2019). The CAMS reanalysis of atmospheric composition. *Atmospheric Chemistry and Physics*, *19*(6), 3515–3556. https://doi.org/10.5194/acp-19-3515-2019

Istomin, V. G. (1963). Absolute concentrations of ion components of the earth's atmosphere at altitudes between 100 and 200 km. *Planetary and Space Science*, *11*(2), 169–172. https://doi.org/10.1016/0032-0633(63)90139-9

Kane, T. J., & Gardner, C. S. (1993). Lidar observations of the meteoric deposition of mesospheric metals. *Science*, *259*(5099), 1297–1300. https://doi.org/10.1126/science.259.5099.1297

Kessler, D. J., & Cour-Palais, B. G. (1978). Collision frequency of artificial satellites: The creation of a debris belt. *Journal of Geophysical Research*, *83*(A6), 2637–2646. https://doi.org/10.1029/JA083iA06p02637

Kissel, J., Brownlee, D. E., Buchler, K., Clark, B. C., Fechtig, H., Grun, E., et al. (1986). Composition of comet Halley dust particles from Giotto observations. *Nature*, *321*, 336–337. https://doi.org/10.1038/321336a0

Klecker, B., Möbius, E., Hovestadt, D., Scholer, M., Gloeckler, G., & Ipavich, F. M. (1986). Discovery of energetic molecular ions (NO^+ and O_2^+) in the storm time ring current. *Geophysical Research Letters*, *13*(7), 632–635. https://doi.org/10.1029/GL013i007p00632

Kopp, E. (1997). On the abundance of metal ions in the lower ionosphere. *Journal of Geophysical Research*, *102*(A5), 9667–9674. https://doi.org/10.1029/97JA00384

Korth, A., Richter, A. K., Loidl, A., Guttler, W., Anderson, K. A., Carlson, C. W., et al. (1987). The heavy ion analyzer PICCA for the comet Halley fly-by with giotto. *Journal of Physics E Scientific Instruments*, *20*(6), 787–792. https://doi.org/10.1088/0022-3735/20/6/037

Kremser, G., Woch, J., Mursula, K., Tanskanen, P., Wilken, B., & Lundin, R. (1995). Origin of energetic ions in the polar cusp inferred from ion composition measurements by the Viking satellite. *Annals of Geophysics*, *13*(6), 595–607. https://doi.org/10.1007/s00585-995-0595-9

Kronberg, E., Daly, P. W., & Vilenius, E. (2020). *Calibration report of the RAPID measurements in the Cluster Science Archive (CSA), technical report*. European Space Agency.

Kumar, S., & Hanson, W. B. (1980). The morphology of metallic ions in the upper atmosphere. *Journal of Geophysical Research*, *85*(A12), 6783–6801. https://doi.org/10.1029/JA085iA12p06783

Laakso, H., Perry, C., McCaffrey, S., Herment, D., Allen, A. J., Harvey, C. C., et al. (2010). Cluster active archive: Overview. *Astrophysics and Space Science Proceedings*, *11*, 3–37. https://doi.org/10.1007/978-90-481-3499-1_1

Lepidi, S., Villante, U., Lazarus, A. J., Szabo, A., & Paularena, K. (1996). Observations of bow shock motion during times of variable solar wind conditions. *Journal of Geophysical Research*, *101*(A5), 11107–11124. https://doi.org/10.1029/96JA00478

Le Roy, L., Altwegg, K., Balsiger, H., Berthelier, J.-J., Bieler, A., Briois, C., et al. (2015). Inventory of the volatiles on comet 67P/Churyumov-Gerasimenko from Rosetta/ROSINA. *Astronomy and Astrophysics*, *583*, A1. https://doi.org/10.1051/0004-6361/201526450

Meyer, L., Klein, M., & Wedell, R. (1977). The energy-angle distribution of heavy particles penetrating solids. *Physica Status Solidi B Basic Research*, *83*(2), 451–463. https://doi.org/10.1002/pssb.2220830211

Mitchell, D. G., Roelof, E. C., & Bame, S. J. (1983). Solar wind iron abundance variations at speeds ≥ 600 km s^{-1}, 1972–1976. *Journal of Geophysical Research*, *88*(A11), 9059–9068. https://doi.org/10.1029/JA088iA11p09059

Moore, T. E., & Horwitz, J. L. (2007). Stellar ablation of planetary atmospheres. *Reviews of Geophysics*, *45*(3), RG3002. https://doi.org/10.1029/2005RG000194

Nakamura, T., Noguchi, T., Tanaka, M., Zolensky, M. E., Kimura, M., Tsuchiyama, A., et al. (2011). Itokawa dust particles: A direct link between s-type asteroids and ordinary chondrites. *Science*, *333*(6046), 1113. https://doi.org/10.1126/science.1207758

Okada, T., Shirai, K., Yamamoto, Y., Arai, T., Ogawa, K., Hosono, K., & Kato, M. (2006). X-ray fluorescence spectrometry of asteroid itokawa by hayabusa. *Science*, *312*(5778), 1338–1341. https://doi.org/10.1126/science.1125731

Paschmann, G., Haaland, S. E., Phan, T. D., Sonnerup, B. U. Ö., Burch, J. L., Torbert, R. B., et al. (2018). Large-scale survey of the structure of the dayside magnetopause by MMS. *Journal of Geophysical Research*, *123*, 2018–2033. https://doi.org/10.1002/2017JA025121

Perry, C. H., Grande, M., Zurbuchen, T. H., Hefti, S., Gloeckler, G., Fennell, J. F., et al. (2000). Use of Fe charge state changes as a tracer for solar wind entry to the magnetosphere. *Geophysical Research Letters.*, *27*(16), 2441–2444. https://doi.org/10.1029/2000GL003780

Phan, T. D., Bale, S. D., Eastwood, J. P., Lavraud, B., Drake, J. F., Oieroset, M., et al. (2020). Parker solar probe in situ observations of magnetic reconnection exhausts during encounter 1. *Astrophysical Jounal*, *246*(2), 34. https://doi.org/10.3847/1538-4365/ab55ee

Phan, T. D., Gosling, J. T., Davis, M. S., Skoug, R. M., Øieroset, M., Lin, R. P., et al. (2006). A magnetic reconnection X-line extending more than 390 Earth radii in the solar wind. *Nature*, *439*(7073), 175–178. https://doi.org/10.1038/nature04393

Plane, J. M. C., Bailey, S. M., Baumgarten, G., & Rapp, M. (2015). Layered phenomena in the mesopause region. *Journal of Atmospheric and Solar-Terrestrial Physics*, *127*, 1–2. https://doi.org/10.1016/j.jastp.2015.04.008

Plane, J. M. C., Cox, R. M., & Rollason, R. J. (1999). Metallic layers in the mesopause and lower thermosphere region. *Advances in Space Research*, *24*(11), 1559–1570. https://doi.org/10.1016/S0273-1177(99)00880-7

Poppe, A. R., Fillingim, M. O., Halekas, J. S., Raeder, J., & Angelopoulos, V. (2016). ARTEMIS observations of terrestrial ionospheric molecular ion outflow at the moon. *Geophysical Research Letters*, *43*, 6749–6758. https://doi.org/10.1002/2016GL069715

Prinsloo, P. L., Strauss, R. D., & le Roux, J. A. (2019). Acceleration of solar wind particles by traveling interplanetary shocks. *The Astrophysical Journal*, *878*(2), 144. https://doi.org/10.3847/1538-4357/ab211b

Reames, D. V., Meyer, J. P., & von Rosenvinge, T. T. (1994). Energetic-particle abundances in impulsive solar flare events. *Astrophysical Journal Supplement*, *90*, 649. https://doi.org/10.1086/191887

Reinhard, R. (1986). The Giotto experiments. *ESA Journal*, *46*, 41–51.

Sagdeev, R. Z., Kissel, J., Bertaux, J. L., Angarov, V. N., Blamont, J. E., Buchler, K., et al. (1986). The element composition of comet halley dust particles – preliminary results from the VEGA PUMA analyzers. *Soviet Astronomy Letters*, *12*, 254.

Schonfeld, S. J., White, S. M., Henney, C. J., Arge, C. N., & McAteer, R. T. J. (2015). Coronal sources of the solar $F_{10.7}$ radio flux. *The Astrophysical Journal*, *808*(1), 29. https://doi.org/10.1088/0004-637X/808/1/29

Seki, K., Keika, K., Kasahara, S., Yokota, S., Hori, T., Asamura, K., et al. (2019). Statistical properties of molecular ions in the ring current observed by the arase (ERG) satellite. *Geophysical Research Letters*, *46*(15), 8643–8651. https://doi.org/10.1029/2F2019GL084163

Sergeev, V., Runov, A., Baumjohann, W., Nakamura, R., Zhang, T. L., Volwerk, M., et al. (2003). Current sheet flapping motion and structure observed by cluster. *Geophysical Research Letters*, *30*(6), 1327. https://doi.org/10.1029/2002GL016500

Shelley, E. G., Johnson, R. G., & Sharp, R. D. (1972). Satellite observations of energetic heavy ions during a geomagnetic storm. *Journal of Geophysical Research*, *77*(31), 6104. https://doi.org/10.1029/JA077i031p06104

Solomon, S. C. (1991). Optical aeronomy. *Reviews of Geophysics*, *29*, 1089–1109.

Stüdemann, W., & Wilken, B. (1982). Detection efficiency of a heavy ion time-of-flight spectrometer with thin carbon foils in the start detector. *Review of Scientific Instruments*, *53*(2), 175–180. https://doi.org/10.1063/1.1136948

Sugiura, M. (1964). Hourly values of equatorial dst for the IGY. In *Annals of the international geophysical year* (Vol. *35*). Pergamon Press.

Trattner, K. J., Fuselier, S. A., Peterson, W. K., Chang, S.-W., Friedel, R., & Aellig, M. R. (2001). Origins of energetic ions in the cusp. *Journal of Geophysical Research*, *106*(A4), 5967–5976. https://doi.org/10.1029/2000JA003005

von Steiger, R., Geiss, J., & Gloeckler, G. (1997). Composition of the solar wind. In *Cosmic winds and the heliosphere*, p. 581.

von Steiger, R., Schwadron, N. A., Fisk, L. A., Geiss, J., Gloeckler, G., Hefti, S., et al. (2000). Composition of quasi-stationary solar wind flows from Ulysses/Solar wind ion composition spectrometer. *Journal of Geophysical Research*, *105*(A12), 27217–27238. https://doi.org/10.1029/1999JA000358

von Steiger, R., & Zurbuchen, T. H. (2002). Kinetic properties of heavy solar wind ions from Ulysses-SWICS. *Advances in Space Research*, *30*(1), 73–78. https://doi.org/10.1016/S0273-1177(02)00174-6

von Zahn, U., Höffner, J., & McNeil, W. J. (2002). Meteor trails as observed by lidar. In E. Murad, & I. P. Williams, Eds., *Meteors in the earth's atmosphere*, p. 149.

Werner, R., Guineva, V., Stoeva, P., & Spasov, S. (1989). The spectrum of comet halley obtained by VEGA-2. *Advances in Space Research*, *9*(3), 221–224. https://doi.org/10.1016/0273-1177(89)90264-0

Wilken, B., Axford, W. I., Daglis, I., Daly, P., Guttler, W., Ip, W. H., et al. (1997). RAPID – The imaging energetic particle spectrometer on cluster. *Space Science Reviews*, *79*, 399–473. https://doi.org/10.1023/A:1004994202296

Wilken, B., & Stüdemann, W. (1984). A compact time-of-flight mass-spectrometer with electrostatic mirrors. *Nuclear Instruments and Methods in Physics Research*, *222*(3), 175–180. https://doi.org/10.1016/0167-5087(84)90391-0

Wilken, B., Weiss, W., Stuedemann, W., & Hasebe, N. (1987). The Giotto implanted ion spectrometer (IIS): Physics and techniques of detection. *Journal of Physics E Scientific Instruments*, *20*(6), 778–785. https://doi.org/10.1088/0022-3735/20/6/036

Wüest, M., Evans, D. S., & von Steiger, R. (2007). *Calibration of particle instruments in space physics*. ESA Publications Division (ISBN: 987-92-9221-936-9).

Yau, A. W., & Andre, M. (1997). Sources of ion outflow in the high latitude ionosphere. *Space Science Reviews*, *80*, 1–25. https://doi.org/10.1023/A:1004947203046

Young, D. T., Balsiger, H., & Geiss, J. (1982). Correlations of magnetospheric ion composition with geomagnetic and solar activity. *Journal of Geophysical Research*, *87*(A11), 9077–9096. https://doi.org/10.1029/JA087iA11p09077

Young, P. R. (2005). The Ne/O abundance ratio in the quiet sun. *Journal of Astronomy and Astrophysics*, *444*(2), L45–L48. https://doi.org/10.1051/0004-6361:200500206

Zank, G. P., Li, G., & Verkhoglyadova, O. (2007). Particle acceleration at interplanetary shocks. *Space Science Reviews*, *130*(1–4), 255–272. https://doi.org/10.1007/s11214-007-9214-2

Ziegler, J. F., Ziegler, M. D., & Biersack, J. P. (2010). SRIM – The stopping and range of ions in matter (2010). *Nuclear Instruments and Methods in Physics Research B*, *268*(11–12), 1818–1823. https://doi.org/10.1016/j.nimb.2010.02.091

Zurbuchen, T. H., Fisk, L. A., Gloeckler, G., & von Steiger, R. (2002). The solar wind composition throughout the solar cycle: A continuum of dynamic states. *Geophysical Research Letters*, *29*(9), 1352. https://doi.org/10.1029/2001GL013946

Zurbuchen, T. H., Raines, J. M., Slavin, J. A., Gershman, D. J., Gilbert, J. A., Gloeckler, G., et al. (2011). MESSENGER observations of the spatial distribution of planetary ions near mercury. *Science*, *333*(6051), 1862. https://doi.org/10.1126/science.1211302

Zurbuchen, T. H., Weberg, M., von Steiger, R., Mewaldt, R. A., Lepri, S. T., & Antiochos, S. K. (2016). Composition of coronal mass ejections. *The Astrophysical Journal*, *826*(1), 10. https://doi.org/10.3847/0004-637X/826/1/10